

UC Berkeley

UC Berkeley Previously Published Works

Title

Fatigue-crack propagation behavior in a high-carbon chromium SUJ2 bearing steel: Role of microstructure

Permalink

<https://escholarship.org/uc/item/1nf522bv>

Authors

Kowathanakul, Nopasorn

Yu, Qin

Zhu, Chaoyi

et al.

Publication Date

2022-03-01

DOI

10.1016/j.ijfatigue.2021.106693

Copyright Information

This work is made available under the terms of a Creative Commons Attribution License, available at <https://creativecommons.org/licenses/by/4.0/>

Peer reviewed

Fatigue-Crack Propagation Behavior in a High-Carbon Chromium SUJ2 Bearing Steel: Role of Microstructure

Nopasorn Kowathanakul^{1,2‡}, Qin Yu^{2‡}, Chaoyi Zhu³, Xiaoqing Li³, Andrew M. Minor^{2,3},
Robert O. Ritchie^{2,3*}

¹*Core Technology R&D Center, NSK Ltd., Fujisawa, Kanagawa, 251-8501 Japan*

²*Materials Sciences Division, Lawrence Berkeley National Laboratory, Berkeley, CA 94720, USA*

³*Department of Materials Science and Engineering, University of California, Berkeley, CA 94720, USA*

[‡]These authors contributed equally to this work.

*Corresponding author: roritchie@lbl.gov

Abstract: High-carbon chromium martensite steels are commonly selected for bearing components in the power generation, automotive and aerospace industries where fatigue failure is a major concern. Accordingly, it is of importance to elucidate the structure-property relationships governing the fatigue properties of such bearing steels. Here, the role of microstructure in influencing the fatigue-crack propagation behavior of a high-carbon chromium SUJ2 bearing steel is examined with emphasis on three martensitic structures: (i) a fine-grained (~10 μm) structure with intragranular (but no intergranular) carbides, (ii) a coarser-grained (~25 μm) structure with discontinuous grain-boundary carbides primarily near triple junctions, and (iii) a coarse-grained (~31 μm) structure with continuous grain-boundary carbides. Although growth rates were fairly similar above $\sim 10^{-8}$ m/cycle, significant differences in behavior were observed at lower, near-threshold growth rates; specifically at a load ratio of 0.1, the ΔK_{th} fatigue threshold was increased from 3.8 $\text{MPa}\cdot\text{m}^{1/2}$ in the fine-grained structure to 5.9 to 6.3 $\text{MPa}\cdot\text{m}^{1/2}$ in the two coarser-grained structures. The dominant factor governing such near-threshold behavior was found to be crack-tip shielding from roughness-induced crack closure, which was most pronounced in the coarser-grained structures; additionally, shielding from crack deflection and branching was apparent in these structures as the crack propagated through the network of intersecting martensite lamellae within the coarse grains. Compared to high-strength stainless steels and low-strength carbon steels, the fine-grained SUJ2 steel displays an exceptional combination of high strength and fatigue-crack growth resistance and is considered to be a superior structural alloy for bearing applications.

Keywords: Bearing steels; martensitic structures; fatigue-crack propagation; near-threshold behavior; crack-tip shielding; crack closure

1. Introduction

Roller bearings are used as machine elements in both simple and complex machines, *e.g.*, bicycles, roller skates, turbines, and power transmission, to allow for motion about the shaft and to support axial and radial loads. Because of the nature of the application, the hardness, toughness, fatigue strength, and wear resistance are the primary concerns of the material selection for roller bearings. High-carbon chromium steels were one of the first bearing steels to be used for ball and roller bearings. Carburized steels were developed somewhat later and are commonly used for tapered roller bearings [1]. Some other high-carbon steels have been selected for specific bearing applications, such as SKH4 or M50 of Cr-Mo-V steel for high-speed and high-temperature applications, and SUS440C martensitic stainless steel for corrosive environments at high temperature [2]. Roller bearings can fail in multiple ways in service, such as by flaking, peeling, denting, fracture, fatigue, wear, and corrosion [3], although metal fatigue is invariably the most critical and consequently determines the lifetime of bearings in most applications. The typical scenario is that the highly concentrated stresses that are repeatedly applied during rolling contact can cause the initiation of fatigue cracks beneath the contacting surfaces with their subsequent propagation leading to final failure of the bearings.

Most studies on the fatigue properties of bearing steels [4-19] have focused on clarifying the influence of such variables as inclusion content, residual stresses, lubrication, and temperature, on the stress/strain-life ($S-N$) behavior of bearing steels [10-18]. Only limited data, however, are available on the fatigue-crack growth properties of high-carbon chromium bearing steels. Beswick [19] examined the influence of chemical composition and heat treatment on the K_{Ic} fracture toughness and ΔK_{th} fatigue threshold of the of 52100 steel (which is similar to SUJ2 steel) and found that a 10 vol.% of retained austenite in the martensitic structure led to improved fatigue-crack growth resistance; however, a corresponding decrease in grain size from 12 to 6 μm had essentially no effect on either the fracture toughness or fatigue threshold.

Here we investigate the fatigue-crack propagation behavior of a Japanese Industrial Standard (JIS) SUJ2 steel, which is one of the commonly used high-carbon chromium martensitic steels for roller bearings. The SUJ2 steel can exhibit excellent mechanical properties

with a hardness over 700 HV, a tensile strength in the range of 1570 - 1960 MPa, and a fracture toughness K_{Ic} in the range of 14 - 18 MPa·m^{1/2} [2]. The present study seeks to understand the microstructural origins of fatigue-crack growth behavior in the JIS SUJ2 steel with particular reference to the variation in crack-tip shielding effects [21] caused by the different grain sizes and types of intergranular carbides.

2. Experimental procedures

2.1 Material

The material under study, JIS-SUJ2 steel, is a typical high-carbon chromium bearing steel. Its chemical composition is listed in [Table 1](#), and can be seen to contain a high percentage of carbon (~1 wt.%) and chromium (~1.5 wt.%). Test specimens for uniaxial tensile and fatigue tests were machined from extruded rod using wire electrical discharge machining. The machined specimens were subsequently heat treated *in vacuo* using three different sequences of austenitizing, quench and tempering, as schematically illustrated in [Fig. 1](#).

The first heat treatment, termed HT1 ([Fig. 1a](#)), followed a commercially-used procedure of austenitizing at 840°C for 60 mins, quenching into oil and then tempering at 200°C for 120 mins. This resulted in an average prior-austenite grain size of ~10 μm. To coarsen the microstructure, two-step solution treatments at higher temperatures were used. Specifically, the second heat treatment (HT2) ([Fig. 1b](#)) involved austenitizing for 30 mins at 1000°C followed by another 60 mins at 800°C; samples were then quenched into a salt bath and tempered at 200°C for 120 mins. For the third heat treatment (HT3) ([Fig. 1c](#)), the samples were austenitized at 1000°C for 30 mins and then at 750°C for 60 mins, quenched into a salt bath and similarly tempered at 200°C for 120 mins. The average prior-austenite grain sizes following the HT2 and HT3 heat treatments were, respectively, ~25 μm and ~31 μm. The specific microstructures are described in Section 3.1.

2.2 Mechanical characterization

Uniaxial tensile testing was performed on the three microstructural conditions using rectangular dog-bone shaped specimens, with a gauge cross-section of 1×1.2 mm² and a gauge length of 10 mm, aligned such that the loading direction was along the extrusion direction of the rod. Uniaxial tensile tests were conducted at room temperature on a 10 kN electro-servo

hydraulic 810 MTS load frame (MTS Corp., Eden Prairie, MN, USA) at an engineering strain rate of $8.0 \times 10^{-4} \text{ s}^{-1}$. At least three samples were tested for each condition.

The fracture toughness and the fatigue-crack growth behavior were characterized using compact-tension C(T) specimens, with a width $W = 24 \text{ mm}$, a thickness $B = 5 \text{ mm}$ and a machined notch length $a_0 = 5 \text{ mm}$. As shown in Fig. 2a, the C(T) specimens were machined from the extruded rod with their mid-section surface located at the mid-section of the rod; the notch and hence general crack extension direction were aligned along the diameter of the rod's cross section from the outer surface to the center of the rod. To facilitate the fatigue pre-cracking, a micro-notch with a root radius of $60 \mu\text{m}$ was made by a micro-notching technique involving repeatedly polishing the root of machined notch tip using a razor blade with $1\text{-}\mu\text{m}$ diamond paste under a small force. Before fatigue testing, the specimen surfaces were ground with silicon carbide paper and polished down to a $1\text{-}\mu\text{m}$ surface finish to permit optical observation of the crack on the specimen surface. All tensile and fatigue specimens were heat-treated after machining.

To measure the crack length continuously during fatigue testing, a uniaxial linear-patterned strain gauge, model EA-06-031DE-350/LE (Vishay Precision Group, Raleigh, NC, USA), was attached to the centerline of the back-face of the C(T) specimens perpendicular to the notch direction (Fig. 2a). Crack lengths were calculated from the compliance measurements based on the back-face strain readings during the unloading portion of each cycle, according to the ASTM Standard E647 [20]:

$$\frac{a}{W} = 1.0033 - 2.35U + 1.3694U^2 - 15.294U^3 + 63.182U^4 - 74.42U^5, \quad (1)$$

$$\text{with } U = \frac{1}{\sqrt{|\varepsilon EBW/P|+1}}, \quad (2)$$

where E is the Young's modulus, B is the specimen thickness, ε is the back-face strain, P is the load, a and W are the crack length and the specimen width, respectively. The validity of the calculated crack length is within the range of $0.2 \leq a/W \leq 0.95$ to avoid a significant error from the large deformation displacements. Accordingly, every test was run until $a/W \sim 0.7$ to maintain accuracy. The strain gauge was calibrated and checked during the pre-cracking by measuring the crack lengths on both specimen surfaces after unloading at each step using an optical microscope

to ensure that the calculated crack lengths were consistent with the optically observed crack lengths.

All C(T) specimens were pre-cracked by cyclic loading in ambient air at a frequency of 25 Hz at constant amplitude to lower the stress-intensity range until the plastic-zone size at the crack tip was smaller than the expected plastic-zone size of the test starting point. The ratio of the minimum and maximum load (or stress intensity), *i.e.*, the load ratio R was set at 0.1 during the pre-cracking process. For the purpose of the fracture toughness, K_{Ic} , measurements, the final length of the pre-crack was in the range of $0.45 \leq a/W \leq 0.55$. Tests were carried out at room temperature for each heat-treated condition according to the ASTM Standard E399 [22]. Both pre-cracking and toughness testing were performed on a 10 kN electro-servo hydraulic 810 MTS load frame (MTS Corp., Eden Prairie, MN, USA) operated using an Instron 8800 digital controller (Instron Corp., Norwood, MA, USA).

Specifically, the toughness tests were performed in stroke control at a displacement rate of 0.0167 mm.s^{-1} . All test results for the measurement of the plane-strain fracture toughness K_{Ic} (Table 2) were made at the point of crack instability and were found to be fully valid, in terms of satisfying the ASTM E399 criteria [22] for small-scale yielding and plane-strain conditions.

The fatigue-crack growth testing was conducted under load control at a sinusoidal frequency f of 25 Hz with a load ratio of $R = 0.1$. Mid- and high-range crack-growth rates were characterized under constant-load conditions, *i.e.*, the load amplitude was kept constant, but the stress-intensity range ($\Delta K = K_{\max} - K_{\min}$) increased as the crack propagated (K_{\max} and K_{\min} are, respectively, the maximum and minimum stress intensities each cycle). The near-threshold growth rates, below $\sim 10^{-8}$ to 10^{-9} m/cycle, and the threshold stress-intensity range (ΔK_{th}) were measured under load-shedding conditions. The applied external load was automatically decreased at a rate such that the imposed normalized K -gradient remained above -0.08 mm^{-1} , as per ASTM Standard E647 [20]. The threshold ΔK_{th} was determined when the crack propagation rate was reduced to the range between $\sim 10^{-11}$ and 10^{-10} m/cycle. All fatigue-crack growth data are presented in log-log plots of the crack propagation rate, da/dN , as a function of stress-intensity range, ΔK . Using the Paris law formulation, *i.e.*, $da/dN = C\Delta K^m$, the scaling constant, C , and the Paris exponent, m , were measured in the intermediate range of growth rates ($\sim 10^{-9}$ to $>$

10^{-7} m/cycle). The stress-intensity factor was calculated from the mode I K -solution for the C(T) geometry [20]:

$$K = \frac{P}{B\sqrt{W}} f\left(\frac{a}{W}\right), \quad (3)$$

$$f\left(\frac{a}{W}\right) = \frac{(2+a/W)}{(1-a/W)^{3/2}} \left(0.886 + 4.64\frac{a}{W} - 13.32\left(\frac{a}{W}\right)^2 + 14.72\left(\frac{a}{W}\right)^3 - 5.6\left(\frac{a}{W}\right)^4\right), \quad (4)$$

where the a/W ratio was derived from the dimensionless compliance obtained from measurements of the back-face strain.

The phenomenon of crack closure was observed during the unloading portion of the fatigue cycle; this is associated with premature physical contact between the crack surfaces before the minimum load is reached [23-25]. The onset of closure point can be estimated when the slope of the elastic compliance (or load-displacement) changes during unloading [26]. Although approximate, we used this compliance technique to identify the closure load (P_{cl}) at the starting point of the crack surface contact during unloading. From Eqs. 3 and 4, the corresponding closure stress intensity, K_{cl} , can be estimated. The effective stress-intensity range, ΔK_{eff} , representing the local stress-intensity range actually experienced at the crack tip, was calculated as $\Delta K_{eff} = K_{max} - K_{cl}$ when $K_{cl} > K_{min}$ and $\Delta K_{eff} = \Delta K$ when $K_{cl} \leq K_{min}$.

2.3 Material characterization

The microstructures resulting from the three heat treatments were characterized by polishing samples to a 0.05- μm surface finish, followed by etching with a prior-austenite grain-boundary etchant (ES Laboratory, Glendora, CA, USA) for 30 secs. They were examined using Hitachi S-4300SE/N scanning electron microscope (SEM), operating in the backscatter electron (BSE) mode at 15 kV, and for chemical composition measurements using energy dispersive spectroscopy (EDS) carried out on the Thermo Scientific Scios 2 DualBeam SEM equipped with Oxford Instruments EDS system. For the point scan and 2-D mapping, a beam current of 3 nA, an accelerating voltage of 20 keV, and a working distance of 7 mm were used. In addition, EDS signals were analyzed with the Aztec software using 1024 channels, a dimensionless process time of five, and a dead time of around 20%. To characterize the grain structures, electron backscattered diffraction (EBSD) was further performed using FEI Strata DB235 SEM operated at 20 kV. To image the martensitic structure by transmission electron microscopy (TEM),

samples were mechanically polished down to a thickness of $\sim 200\ \mu\text{m}$ and punched into 3 mm-diameter disks, prior to chemical jet polishing to make them TEM transparent using a Fischione Twin Jet Electropolisher (Model 110) operated at $\sim 20\ \text{V}$ with a chemical solution of 6.8% perchloric acid, 34.7% butanol and 58.5% methanol at -20°C . Scanning transmission electron microscopy (STEM) images were obtained in an FEI TitanX TEM at 300 kV.

After fatigue testing, fractographic analysis was performed on the fracture surface of the broken specimens using secondary electron (SE) imaging with Hitachi S-4300SE/N SEM operating at 5–15 kV. To specifically examine the corresponding crack-path profiles and discern the deformation mechanisms in the vicinity of the crack tip and crack wake under plane-strain conditions, unbroken C(T) specimens were sliced through the thickness at the mid-thickness section. The interior mid-section surface of the half cut was progressively polished to a $0.05\text{-}\mu\text{m}$ surface finish and chemically etched for 30 sec to highlight the prior-austenite grain boundaries. Crack-path profiles were characterized using Thermo Scientific Scios 2 DualBeam SEM operating in the SE mode at 10 kV.

3. Results and discussion

3.1 Microstructures

The three microstructures of the SUJ2 bearing steel under study are shown in Fig. 3, based on BSE imaging and EDS measurements. Heat treatment HT1, consisting of an 840°C solution treatment, oil quench and 200°C temper, resulted in an equiaxed lamellar-type martensitic structure with a prior-austenite grain size of $10 \pm 2\ \mu\text{m}$ (Fig. 3a). The thickness of the martensitic lamellar was $59 \pm 16\ \text{nm}$ (Fig. 3b and Fig. S1a), with spherical and elliptical FeCr-rich carbides mainly found inside the grains (Fig. 3c). With the higher austenitizing temperature in the HT2 heat treatment, the prior-austenite grain size increased to $25 \pm 7\ \mu\text{m}$ (Fig. 3d and Fig. S1b), with a network of intersecting martensitic lamellar, with a thickness of $544 \pm 158\ \text{nm}$, developed within the grains (Fig. 3e and Figs. S1b, d). Unlike HT1, necklace-shaped Fe-rich carbides were formed along the grain boundaries after HT2 but were mostly distributed in the vicinity of the triple junctions (Fig. 3f). For the HT3 heat treatment, the grain size increased to $31 \pm 7\ \mu\text{m}$ whereas the thickness of intersecting martensitic lamellar was $366 \pm 123\ \text{nm}$ (Fig. 3g and Fig. S1c). Compared to HT2, essentially continuous Fe-rich carbides were developed along almost all the grain boundaries after HT3 (Figs. 3h and i).

3.2 Tensile properties and fracture toughness

Figure 4 presents the uniaxial engineering stress-strain curves characterized for the three heat-treated SUJ2 bearing steels. The tensile properties, along with the measured fracture toughnesses, are listed in Table 2. Results for the HT1 microstructure indicated a high yield strength (σ_y) of 1940 MPa, although the subsequent extent of plasticity was limited with the samples fracturing at a tensile strength (σ_{uts}) of 2074 MPa after a total elongation (ϵ_f) of 1.4%. The HT2 and HT3 structures with their 2- to 3-fold larger prior-austenite grain sizes, however, showed reduced tensile strengths of, respectively, 798 and 930 MPa, with ductilities in the range of 0.45% and 0.56%, *i.e.*, 60 to 70% lower than the HT1 structure. Fracture toughness, K_{Ic} , values for the three heat-treated conditions were essentially unchanged at 17 MPa·m^{1/2}, 17 MPa·m^{1/2} and 18.3 MPa·m^{1/2} for the HT1, HT2 and HT3 structures, respectively.

3.3 Fatigue-crack propagation behavior

The fatigue-crack propagation behavior of the three heat-treated SUJ2 bearing steels are presented in Fig. 5 in terms of the crack-growth rates (da/dN) from 10⁻¹¹ to >10⁻⁷ m/cycle as a function of the stress-intensity range (ΔK). In contrast to the uniaxial tensile properties, the fatigue-crack growth resistance was found to be improved in the coarser microstructures, specifically when the prior-austenite grain sizes were enlarged from ~10 μm (for HT1) to ~25 μm (HT2) and ~31 μm (HT3). Compared to a value of $\Delta K_{th} = 3.78$ MPa·m^{1/2} in the HT1 microstructure, the ΔK_{th} threshold values were increased by some 60% to 6.29 and 5.93 MPa·m^{1/2} in the HT2 and HT3 structures, respectively. This improvement in the ΔK_{th} thresholds and in the near-threshold crack-growth resistance is attributed to a higher degree of crack-tip shielding due to roughness-induced crack closure in the coarser-grained structures. We will analyze the crack closure effects in the three steel microstructures in Section 3.4 and further discuss possible mechanisms in Section 3.5.

In the intermediate range of growth rates, roughly between ~10⁻⁹ and 10⁻⁷ m/cycle, the Paris exponent for the fine-grained HT1 material was found to be $m \sim 2.2$; corresponding m values for the coarser-grained HT2 and HT3 materials were 3.6 and 3.3, respectively. The microstructural influence at such intermediate and higher growth rates can be seen to be progressively less pronounced compared to that at near-threshold growth rates, consistent with the far larger

difference in crack closure between the three microstructures in the latter regime, as discussed in the following section.

3.4 Crack closure analysis

As noted above, crack closure is a phenomenon associated with fatigue-crack propagation where premature physical contact occurs between the mating crack surfaces during the unloading cycle [23]. The most ubiquitous form of such closure is roughness-induced crack closure, which originates from the contact of the local fracture surface asperities induced by small variations in mode II displacements of the neighboring crack flanks [24]. The effect of roughness-induced crack closure is most potent in the near-threshold regime, where the crack-opening displacements (CODs) are comparable to the size of the surface asperities [21].

Figure 6 compares the variation in the degree of crack closure, defined as the ratio of the closure stress intensity to the maximum stress intensity, K_{cl}/K_{max} , as a function of the stress-intensity range (ΔK) for the three heat-treated structural conditions. At intermediate growth rates, where ΔK is typically in the range of ~ 8 to $14 \text{ MPa}\cdot\text{m}^{1/2}$, crack closure effects for all three structures are relatively insignificant, with K_{cl}/K_{max} values under 0.2 and tending towards 0.1 with further increases in ΔK (Fig. 6). However, the effect of crack closure, which diminishes the effective stress-intensity range actually experienced at the crack tip, becomes progressively more pronounced as the ΔK decreases into the near-threshold region, with K_{cl}/K_{max} values reaching 0.3 to 0.45. In addition to the ΔK level, such roughness-induced closure is clearly governed by the fracture surface roughness, which is affected by the coarseness of the grain size. Indeed, it is evident from the experimental measurements in Fig. 6 that the coarser-grained HT2 and HT3 structures display definitively higher levels of crack closure than the HT1 structure as the ΔK_{th} threshold is approached. Furthermore, although the K_{cl}/K_{max} values measured in the HT2 and HT3 samples are of the same order of magnitude, a higher level of crack closure is detectable in the HT2 structure (Fig. 6), which we believe has a microstructural origin as discussed in the following section on fractographic analysis.

The effect of crack closure on the mechanical driving force for crack growth can be approximately quantified by estimating an effective stress-intensity range, ΔK_{eff} , defined as $K_{max} - K_{cl}$ (when $K_{cl} > K_{min}$) and ΔK (when $K_{cl} \leq K_{min}$). Figure 7a shows plots of the fatigue-crack propagation rates, da/dN , as a function of ΔK_{eff} ; additionally, the effective fatigue thresholds,

$(\Delta K_{th})_{eff}$, and the Paris-law constants fit from the da/dN vs. ΔK_{eff} data are listed in Table 3. To visualize the role of crack closure, curves of da/dN vs. ΔK_{eff} and da/dN vs. ΔK are shown for comparison, in Figs. 7b-d for each heat-treated condition. Figure 7a clearly shows how the role of crack closure is relatively minor in the intermediate range of growth rates but, as noted above, it becomes far more pronounced at lower growth rates as the threshold is approached. As a result, in terms of the stress-intensity range, differences in the fatigue-crack growth rate behavior are significantly diminished at near-threshold levels. This is particularly pronounced for the HT2 and HT3 specimens, where their $(\Delta K_{th})_{eff}$ threshold values, after accounting for the crack closure, are practically the same, *i.e.*, $3.98 \text{ MPa}\cdot\text{m}^{1/2}$ and $3.89 \text{ MPa}\cdot\text{m}^{1/2}$, respectively. This implies that the influence of the different microstructures, in particular the coarsened grain size, on fatigue-crack growth in this alloy are primarily manifest through the role of crack closure, although our data indicate that the observed microstructural effects cannot be fully accounted for by our estimation of the closure stress intensities. Part of the reason for this may be associated with the procedure that we used for the measurement of the closure loads. Unloading compliance is clearly an approximate method, yet all techniques that have been used to detect K_{cl} [26] tend to suffer from an inherent lack of precision due to the nature of the closure phenomenon. Additionally, other mechanisms of crack-tip shielding may be *at play*, in particular crack deflection and branching, which would not be fully manifested in the estimation of the closure load.

3.5 Crack-path profiles and fractography

To understand the differences in the fatigue-crack growth resistance of the three heat-treated specimens, it is naturally important to characterize the deformation and fracture modes associated with crack extension. As such, we characterized the crack-path profiles at the mid-thickness section of the fatigue-tested specimens, and used chemical etching to reveal the features of the deformed microstructure in the plastic-wake region, such as the martensitic structure and the presence of grain boundaries and carbides. Figure 8 presents the secondary electron imaging of the crack-path profiles for crack growth in both the near-threshold and the mid-range regimes. In parallel, we characterized the fractographic morphology of the three heat-treated specimens, again both for the near-threshold and the mid-range growth regimes (Fig. 9).

As seen in Fig. 8a, the crack path displays a typical mode-I straight profile near the threshold region for the HT1 specimen which has a fine-grained structure containing intragranular carbides.

The crack propagates predominantly in a transgranular mode within the grains. In particular, the propagating crack tends to cut through the larger carbides with transverse dimensions sized over ~500 nm (blue Arrow A in Fig. 8a). Also, marginal crack deflection occurs as the crack front encounters the spherical carbides with diameters smaller than ~500 nm (red Arrow B in Fig. 8a). The dominant transgranular cracking results in a relatively flat fracture surface near the threshold region (Fig. 9a). As indicated by the red arrows in Fig. 9a, some spherical carbides are exposed on the fracture surface, while some crater sites originating from the carbide detachment are visible. Also detectable are cleaved regions resulting from the cleavage cracking of large-sized carbides (blue arrows in Fig. 9a). In the mid-range regime of crack growth rates (*e.g.*, $\Delta K \sim 5.5 \text{ MPa}\cdot\text{m}^{1/2}$ in Fig. 8b), although the majority of the crack extension is still transgranular, short crack segments can be detected to align along the grain boundaries (red arrows Fig. 8b), indicating that a mixture of transgranular and intergranular cracking can occur in the mid-range growth rates in the HT1 structure. This observation is further confirmed by the examination of the fatigue fracture surface at $\Delta K \sim 8 \text{ MPa}\cdot\text{m}^{1/2}$ (Fig. 9b) where a mixed morphology of transgranular features with minor intergranular features is in evidence.

Near-threshold crack growth in the coarse-grained HT2 structure involves both transgranular and intergranular fracture. As is evident in Fig. 8c, the intergranular cracking is likely to be nucleated at the necklace-shaped carbides, which are discontinuously distributed at the grain boundaries in this structure, particularly in the vicinity of the triple junctions. Indeed, a large portion of the fatigue fracture surface in Fig. 9c, which is close to the threshold, is intergranular where the remaining carbides can be clearly detected (dashed red circle in Fig. 9c). Additionally, marked crack deflection is apparent as the crack propagates through the intersected martensitic lamellae within the grains (purple arrow A in Fig. 8c). In short, the combined effects of intergranular cracking and martensite-induced crack deflection in the HT2 structure leads to pronounced variations in the crack path which roughen the crack surfaces and in turn result in a higher degree of crack closure; accordingly, this structure exhibits a 66% higher ΔK_{th} threshold than that in the stronger HT1 structure. There is also a mixture of transgranular and intergranular cracking in higher (intermediate) growth rates in the HT2 structure, which can be readily seen in both the crack-path profiles (Fig. 8d) and directly on the fatigue fracture surfaces (Fig. 9d).

Corresponding crack-path profiles for the HT3 structure are shown in Fig. 8e where in the near-threshold regime, crack propagation is predominantly transgranular with only minor evidence of an intergranular mode. Such a transgranular crack path results in a less tortuous crack trajectory in this structure compared to that in the HT2 structure (Fig. 8d), that is confirmed in images of the fatigue fracture surfaces which display a relatively flat morphology with dominant transgranular features (Fig. 9e). We believe that, compared to the HT2 structure, this observation that crack paths are not as rough in the HT3 structure is the probable cause of its somewhat smaller closure levels and the ~6% lower fatigue threshold (Table 3). At the intermediate range of growth rates, however, crack-path profiles (Fig. 8f) and the fracture surface morphology (Fig. 9f) in the HT3 structure are largely similar to that in the HT2 structure with a mix of intergranular and transgranular cracking.

3.6 Comparison to other steels

Figure 10 compares the fatigue-crack growth properties of the three heat-treated SUJ2 bearing steels to those of other structural steels [27-30]. The tensile properties along with the fatigue threshold of each steel are summarized in Table 4. The quoted fatigue thresholds were all measured in room temperature at an R ratio of either 0.05 or 0.1.

As shown in Fig. 10 and Table 4, the fine-grained SUJ2 bearing steel can be seen to possess an excellent combination of ultrahigh strength and fatigue crack-growth resistance. Specifically, the fatigue crack-growth behavior of the fine-grained SUJ2 steel (HT1) is comparable to that of the fine-grained (quenched and 200°C tempered) 300-M steel [29] at a similar (~2 GPa) tensile strength, and exhibits ΔK_{th} fatigue thresholds that are ~26% higher than those in 300-M regardless of grain size; however, the 300-M steel is much tougher. Compared to the fine-grained SUJ2 steel, the tensile strengths of the coarser-grained microstructures in the SUJ2 steel (HT2, HT3) are far lower, *i.e.*, ~800 MPa (HT2) and 930 MPa (HT3), but their fatigue thresholds are, respectively, ~66% and ~57% higher. High-strength Fe-4Cr-0.35C austenitic stainless steels [29] and martensitic 410 stainless steels [30] have fatigue thresholds that fall in between those of the fine-grained and coarse-grained SUJ2 steel, but none of these high-strength steels can match the high ΔK_{th} thresholds reported for low-strength plain carbon steels, such as AISI 1005 [27] and AISI 1055 [28] (Fig. 10). However, clearly such low-strength alloys would be unsuitable as bearing materials.

Overall, it is concluded that the SUJ2 bearing steel, with the appropriate microstructure, can outperform most high-strength steels in terms of an excellent combination of tensile strength and fatigue-crack growth properties, which justifies its selection as a superior structural alloy for bearing applications.

4. Conclusions

This work describes an experimental study of the fatigue-crack propagation properties of the high-carbon chromium SUJ2 bearing steel, heat-treated into three microstructural conditions. Based on room-temperature measurements at an R ratio of 0.1 over a range of crack growth rates from $\sim 10^{-11}$ to $> 10^{-7}$ m/cycle, the following main conclusions can be made:

- In terms of mechanical properties, the SUJ2 bearing steel, austenitized at 840°C, oil quenched and tempered at 200°C with fine 10 μm prior-austenite grain size, displays an ultrahigh tensile strength of over 2 GPa with a ΔK_{th} fatigue threshold of 3.8 $\text{MPa}\cdot\text{m}^{1/2}$. The use of higher and two-step austenitizing treatments which increase the prior-austenite grain size, can enhance the fatigue-crack propagation resistance but at the severe expense of tensile strength and ductility; the plane-strain K_{Ic} fracture toughness, however, remains essentially unchanged.
- For bearings which operate in the very high cycle fatigue region, the fatigue-crack growth threshold stress intensities and fatigue-crack growth rates in the vicinity of these thresholds are of particular significance as it is this regime of fatigue behavior that can dominate the estimation of conservative lifetimes.
- The value of the ΔK_{th} fatigue threshold in this bearing steel appears to be significantly affected by the prior-austenite grain size. The ΔK_{th} value for the fine-grained (~ 10 μm) HT1 structure was 3.8 $\text{MPa}\cdot\text{m}^{1/2}$, whereas ΔK_{th} values of the coarser-grained structures were 6.3 $\text{MPa}\cdot\text{m}^{1/2}$ (HT2) and 5.9 $\text{MPa}\cdot\text{m}^{1/2}$ (HT3) where the grain sizes were ~ 25 μm and ~ 31 μm , respectively.
- Roughness-induced crack closure, involving premature contact of the crack surfaces during unloading, is deemed to play the salient mechanistic role in enhancing the fatigue thresholds in the coarser-grained HT2 and HT3 microstructures. For the all-important near-threshold growth rate behavior, unlike the mainly transgranular cracking mode in the fine-grained HT1 structure, a rougher mixed intergranular/transgranular cracking mode was observed in the

coarser-grained structures which induced a higher degree of crack-tip shielding due to crack closure. In addition, crack deflection and branching was observed where the crack propagated through the intersecting martensitic lamellae, which served to further enhance the crack-tip shielding.

- The higher degree of crack closure at near-threshold levels and the correspondingly slightly improved fatigue resistance of the HT2, compared to the HT3, structure appears to result from the increased tendency of intergranular cracking in the HT2 structure due to the necklace-shaped carbides that are discontinuously distributed along the grain boundaries, especially in the vicinity of the triple junctions.
- The high-carbon chromium SUJ2 steel outperforms high-strength stainless steels and low-strength carbon steels in terms of a combination of ultrahigh strength and fatigue-crack growth resistance. Considering its combination of tensile strength and fatigue-crack growth properties, the SUJ2 steel is an excellent alloy steel for bearing applications.

Acknowledgments

This study was funded by a grant to the University of California from NSK Ltd., Japan. X.L. and C.Z. acknowledge support from the U.S. Office of Naval Research under Grant No. N00014-17-1-2283. Work at the Molecular Foundry was supported by the Office of Science, Office of Basic Energy Sciences, of the U.S. Department of Energy under Contract No. DE-AC02-05CH11231.

References

- [1] Harris, T.A., & Kotzalas, M.N., 2006. Essential Concepts of Bearing Technology (5th ed.). CRC Press. <https://doi.org/10.1201/9781420006599>
- [2] NSK Ltd., Japan., 1991. Catalog No. E728g: Technical Report. [updated 2012]. https://www.nsk.com/common/data/ctrGPdf/bearings/e728g.pdf?_ga=2.173605411.1863808255.1636602279-1136026872.1636602279
- [3] NSK Ltd., Japan., 1997. Catalog No. E7005c: New Bearing Doctor. [updated 2014]. https://www.nsk.com/common/data/ctrGPdf/bearings/e7005c.pdf?_ga=2.173147555.1863808255.1636602279-1136026872.1636602279

- [4] Syniuta, W.D., Corrow, C.J., 1970. Scanning electron microscope studies of fracture mechanisms of SAE 52100 bearing steel. *Wear* 15, 171–186. [https://doi.org/10.1016/0043-1648\(70\)90192-4](https://doi.org/10.1016/0043-1648(70)90192-4)
- [5] Stickels, C.A., 1974. Carbide refining heat treatments for 52100 bearing steel. *Metall. Mater. Trans. B* 5, 865–874. <https://doi.org/10.1007/BF02643140>
- [6] Nakazawa, K., Krauss, G., 1978. Microstructure and fracture of 52100 steel. *Metall. Trans. A* 9, 681–689. <https://doi.org/10.1007/BF02659925>
- [7] Bhadeshia, H.K.D.H., 2012. Steels for bearings. *Progr. Mater. Sci.* 57, 268–435. <https://doi.org/10.1016/J.PMATSCI.2011.06.002>
- [8] Hwang, H., de Cooman, B.C., 2016. Influence of the initial microstructure on the spheroidization of SAE 52100 bearing steel. *Steel Res. Intl.* 87, 112–125. <https://doi.org/10.1002/srin.201400591>
- [9] Lu, X., Qian, D., Li, W., Jin, X., 2019. Enhanced toughness of bearing steel by combining prior cold deformation with martensite pre-quenching and bainite transformation. *Mater. Lett.* 234, 5–8. <https://doi.org/10.1016/J.MATLET.2018.09.017>
- [10] Schlicht, H., Schreiber, E., Zwirlein, O., 1988. Effects of material properties on bearing steel fatigue strength, in: Hoo, J.J.C. (Ed.), *Effect of Steel Manufacturing Processes on the Quality of Bearing Steels*. ASTM International, West Conshohocken, PA, 81–101. <https://doi.org/10.1520/STP26228S>
- [11] Furumura, K., Murakami, Y., Abe, T., 1998. Case-hardening medium carbon steel for tough and long life bearing under severe lubrication conditions, in: Hoo, J.J.C., Green, W.B. (Eds.), *Bearing Steels: Into the 21st Century*. ASTM International, West Conshohocken, PA, 293–306. <https://doi.org/10.1520/STP12135S>
- [12] Shiozawa, K., Lu, L., Ishihara, S., 2001. S–N curve characteristics and subsurface crack initiation behaviour in ultra-long life fatigue of a high carbon-chromium bearing steel. *Fat. Fract. Engin. Mater. Struct.* 24, 781–790. <https://doi.org/10.1046/j.1460-2695.2001.00459.x>

- [13] Goto M. 2008. Development of long life case-hardened bearing steel with rust resistance. *JTEKT Engineering Journal* (English Edition) No. 1004E, 23-27. http://eb-cat.ds-navi.co.jp/enu/jtekt/tech/ej/img/no1004E/1004e_05.pdf
- [14] Kerscher, E., Lang, K.H., Löhe, D., 2008. Increasing the fatigue limit of a high-strength bearing steel by thermomechanical treatment. *Mater. Sci. Eng. A* 483–484, 415–417. <https://doi.org/10.1016/J.MSEA.2006.09.170>
- [15] Mayer, H., Haydn, W., Schuller, R., Issler, S., Furtner, B., Bacher-Höchst, M., 2009. Very high cycle fatigue properties of bainitic high carbon–chromium steel. *Int. J. Fatigue* 31, 242–249. <https://doi.org/10.1016/J.IJFATIGUE.2008.09.001>
- [16] Murakami, Y., 2012. Material defects as the basis of fatigue design. *Int. J. Fatigue* 41, 2–10. <https://doi.org/10.1016/J.IJFATIGUE.2011.12.001>
- [17] Karsch, T., Bomas, H., Zoch, H.W., Mändl, S., 2014. Influence of hydrogen content and microstructure on the fatigue behaviour of steel SAE 52100 in the VHCF regime. *Int. J. Fatigue* 60, 74–89. <https://doi.org/10.1016/J.IJFATIGUE.2013.09.006>
- [18] Matsunaga, H., Komata, H., Yamabe, J., Fukushima, Y., Matsuoka, S., 2014. Effect of size and depth of small defect on the rolling contact fatigue strength of bearing steel JIS-SUJ2. *Procedia Mater. Sci.* 3, 1663–1668. <https://doi.org/10.1016/J.MSPRO.2014.06.268>
- [19] Beswick, J.M., 1989. Fracture and fatigue crack propagation properties of hardened 52100 steel. *Metall. Trans. A* 20, 1961–1973. <https://doi.org/10.1007/BF02650283>
- [20] ASTM E647-15e1, Standard Test Method for Measurement of Fatigue Crack Growth Rates, ASTM International, West Conshohocken, PA, 2015, www.astm.org
- [21] Ritchie, R.O., 1988. Mechanisms of fatigue crack propagation in metals, ceramics and composites: Role of crack tip shielding. *Mater. Sci. Eng. A* 103, 15–28. [https://doi.org/10.1016/0025-5416\(88\)90547-2](https://doi.org/10.1016/0025-5416(88)90547-2)
- [22] ASTM E399-20a, Standard Test Method for Linear-Elastic Plane-Strain Fracture Toughness of Metallic Materials, ASTM International, West Conshohocken, PA, 2020, www.astm.org

- [23] Elber, W., 1971. The significance of fatigue crack closure, in: Rosenfeld, M.S. (Ed.), *Damage Tolerance in Aircraft Structures*. ASTM International, West Conshohocken, PA, pp. 230–242. <https://doi.org/10.1520/STP26680S>
- [24] Suresh, S., Ritchie, R.O., 1982. A geometric model for fatigue crack closure induced by fracture surface roughness. *Metall. Trans. A* 13, 1627–1631. <https://doi.org/10.1007/BF02644803>
- [25] Pippan, R., Hohenwarter, A., 2017. Fatigue crack closure: A review of the physical phenomena. *Fat. Fract. Engin. Mater. Struct.* 40, 471–495. <https://doi.org/10.1111/ffe.12578>
- [26] Allison, J.E., Ku, R.C., Pompetzki, M.A., 1988. A comparison of measurement methods and numerical procedures for the experimental characterization of fatigue crack closure, in: Newman, J.C., Elber, W. (Eds.), *Mechanics of Fatigue Crack Closure*. ASTM International, West Conshohocken, PA, 171–185. <https://doi.org/10.1520/STP27207S>
- [27] Benson, J.P., 1979. Influence of grain size and yield strength on threshold fatigue behaviour of low-alloy steel. *Met. Sci.* 13, 535–539. <https://doi.org/10.1179/030634579790438282>
- [28] Cooke, R.J., Beevers, C.J., 1974. Slow fatigue crack propagation in pearlitic steels. *Mater. Sci. Eng.* 13, 201–210. [https://doi.org/10.1016/0025-5416\(74\)90191-8](https://doi.org/10.1016/0025-5416(74)90191-8)
- [29] Ritchie, R.O., 1977. Near-threshold fatigue crack propagation in ultra-high strength steel: Influence of load ratio and cyclic strength. *J. Engin Mater Technol., Trans. ASME Ser. H* 99, 195–204. <https://doi.org/10.1115/1.3443519>
- [30] Stanzl-Tschegg, S., Schönbauer, B., 2010. Near-threshold fatigue crack propagation and internal cracks in steel. *Procedia Engin.* 2, 1547–1555. <https://doi.org/10.1016/J.PROENG.2010.03.167>

Table 1. Chemical compositions (wt.%) of the high carbon-chromium bearing steel, JIS-SUJ2 [2].

Fe	C	Cr	Mn	Si	P	S
Balance	0.95-1.10	1.30-1.60	0.50	0.15-0.35	0.025	0.025

Table 2. Microstructural features, tensile properties and fracture toughness values for the three heat-treated SUJ2 bearing steels.

Heat treatment	Grain size (μm)	Martensite lamellar thickness (nm)	Yield strength σ_y (MPa)	Tensile strength σ_{uts} (MPa)	Total elongation ϵ_f (%)	Fracture toughness K_{Ic} (MPa $\cdot\text{m}^{1/2}$)
HT1	10 \pm 2	59 \pm 16	1940 \pm 37	2074 \pm 114	1.40 \pm 0.16	17.0 \pm 0.6
HT2	25 \pm 7	544 \pm 158	<i>n.a.</i>	798 \pm 67	0.45 \pm 0.05	17.0 \pm 1.6
HT3	31 \pm 7	366 \pm 123	<i>n.a.</i>	930 \pm 43	0.56 \pm 0.02	18.3 \pm 0.6

Table 3. Experimental results pertaining to fatigue-crack propagation behavior in the three heat-treated SUJ2 bearing steels.

Heat treatment	Grain size (μm)	Paris law constants		ΔK_{th} (MPa $\cdot\text{m}^{1/2}$)	Paris law constants		$(\Delta K_{\text{th}})_{\text{eff}}$ (MPa $\cdot\text{m}^{1/2}$)
		C	m		$(C)_{\text{eff}}$	$(m)_{\text{eff}}$	
HT1	10 \pm 2	1.0×10^{-10}	2.19	3.78	6.0×10^{-11}	2.63	2.83
HT2	25 \pm 7	4.0×10^{-12}	3.61	6.29	4.0×10^{-11}	2.63	3.98
HT3	31 \pm 7	7.0×10^{-10}	3.28	5.93	4.0×10^{-11}	2.62	3.89

* Note that the units used for the calculation of the scaling constants C and $(C)_{\text{eff}}$ are m/cycle and MPa $\cdot\text{m}^{1/2}$.

Table 4. Comparison of the fatigue-crack growth behavior for the three-heat treated SUJ2 bearing steels with other steels tested with $R = 0.1$ at room temperature.

Material	Grain size (μm)	Yield strength σ_y (MPa)	Tensile strength σ_{uts} (MPa)	Fatigue threshold ΔK_{th} (MPa $\cdot\text{m}^{1/2}$)	Ref.
SUJ2 bearing steel	10	1940	2074	3.8	-
	25	<i>n.a.</i>	798	6.3	
	31	<i>n.a.</i>	930	5.9	
1005 carbon steel	24	411	490	9	[27]
	70	368	505	12	
1055 carbon steel*	27	399	917	12.9	[28]
300-M steel*	20	1737	2006	3.0	[29]
	160	1657	1986	3.1	
Fe-4Cr-0.35C steel*	30	1300	<i>n.a.</i>	4.4	[29]
410 stainless steel	9	610	800	4.0	[30]

*1055 carbon steel [28], 300-M steel [29] and Fe-4Cr-0.35C steel [29] were fatigue tested at R -ratio of 0.05 at room temperature.

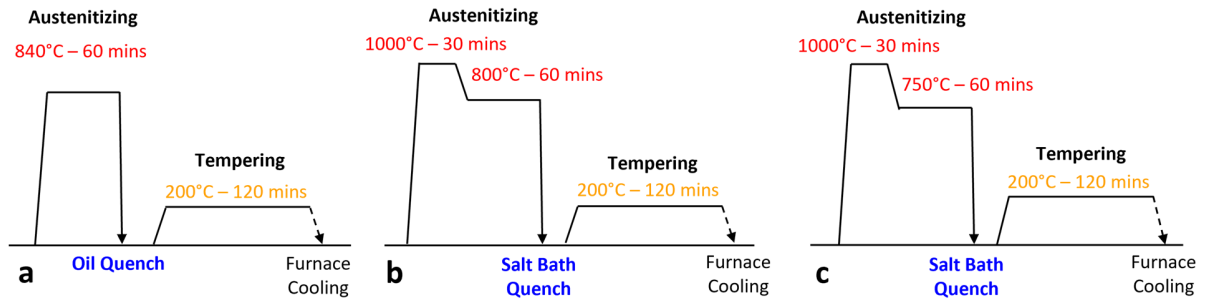


Fig. 1. The three heat treatments (HTs) of austenitizing, quenching, and tempering used to change the microstructure of the SUJ2 bearing steel: (a) HT1, (b) HT2 and (c) HT3.

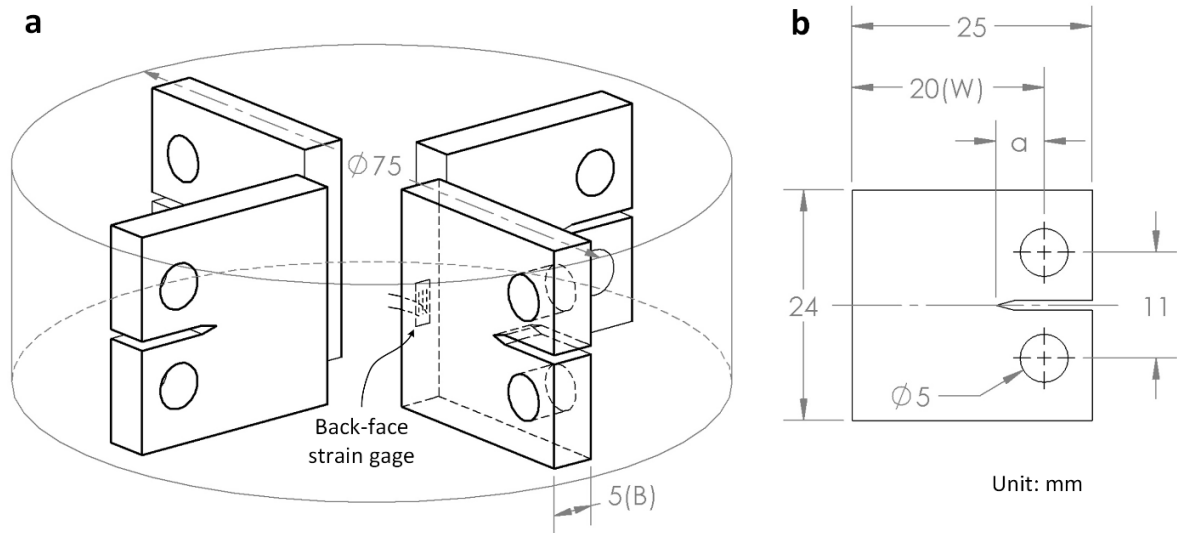


Fig. 2. Compact-tension C(T) specimens used for the fracture toughness and fatigue-crack growth studies: (a) orientation of C(T) specimens in the extruded steel rod. (b) dimensions of the C(T) specimen.

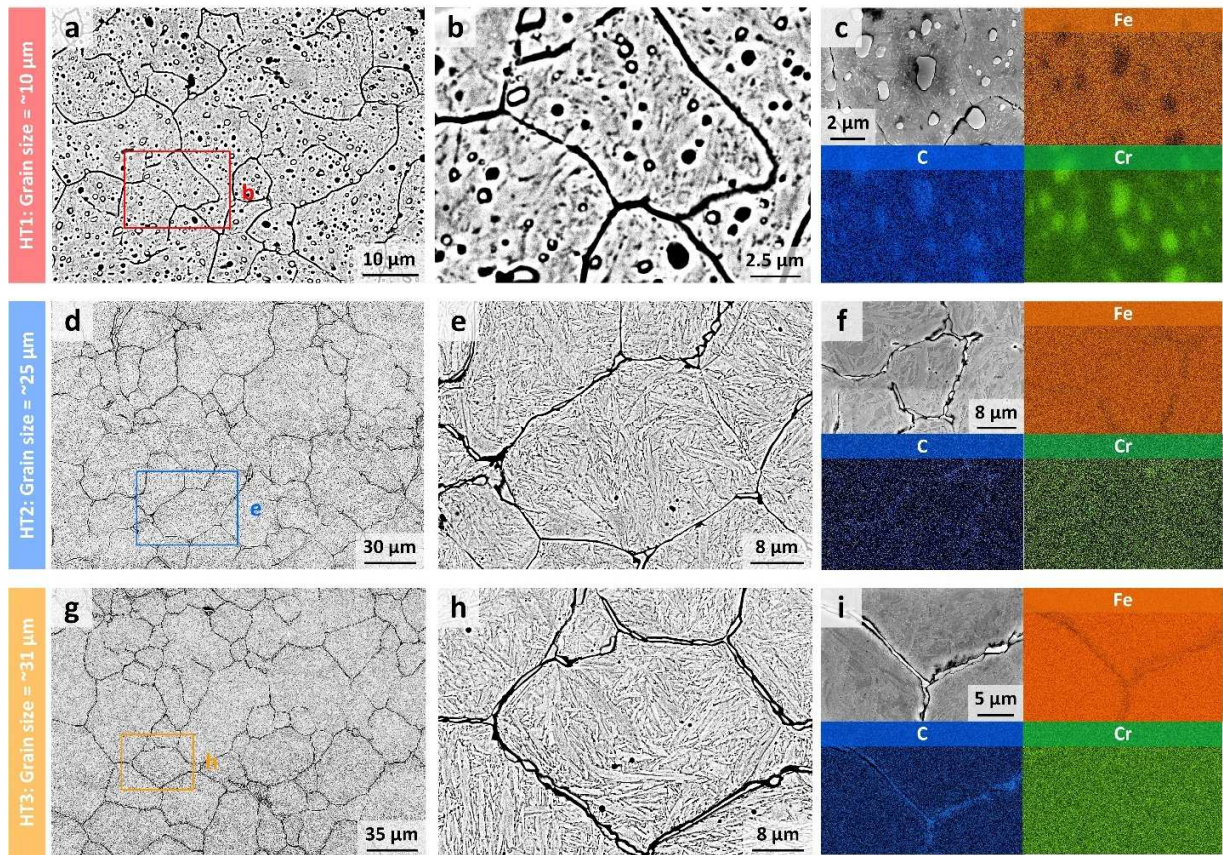


Fig. 3. Microstructures of the three heat-treated SUJ2 bearing steels. (a, b) BSE images taken from the HT1 specimen showing a lamellar-structured martensite with an average prior-austenite grain size of $\sim 10 \mu\text{m}$. (c) Spherical and elliptical FeCr-rich carbides are predominantly developed inside the grains. (d, e) BSE images taken from the HT2 specimen showing a lamellar-structured martensite with an average prior-austenite grain size of $\sim 25 \mu\text{m}$. (f) Intergranular Fe-rich carbides are observed mostly in the vicinity near the triple joints. (g, h) BSE images taken from the HT3 specimen showing a lamellar-structured martensite with an average prior-austenite grain size of $\sim 31 \mu\text{m}$. (i) Relatively continuous intergranular Fe-rich carbides are developed along almost all the grain boundaries.

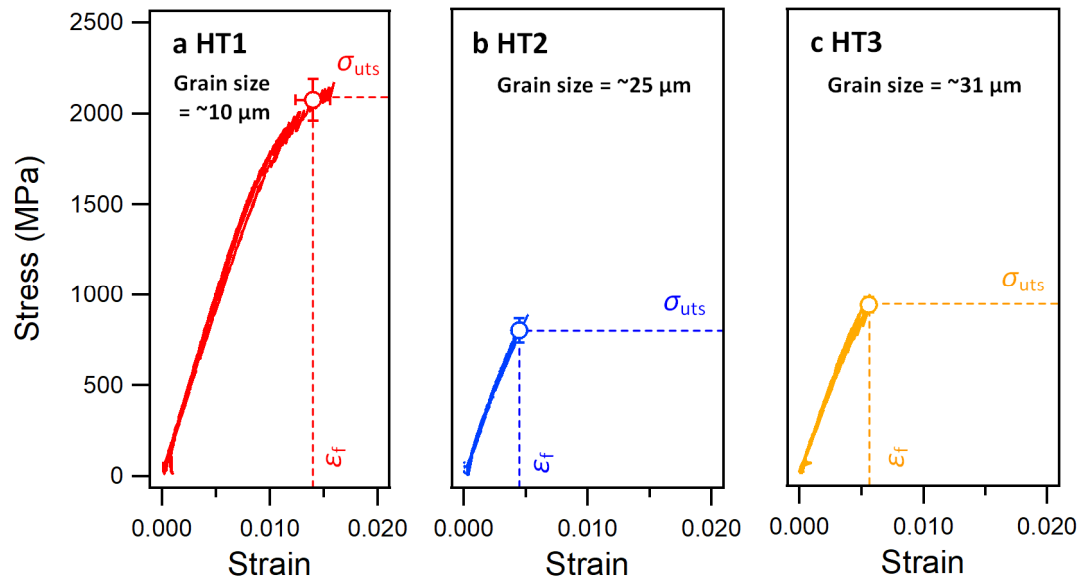


Fig. 4. Uniaxial tensile stress-strain curves for the three heat-treated SUJ2 bearing steels: (a) HT1, (b) HT2, and (c) HT3 microstructures.

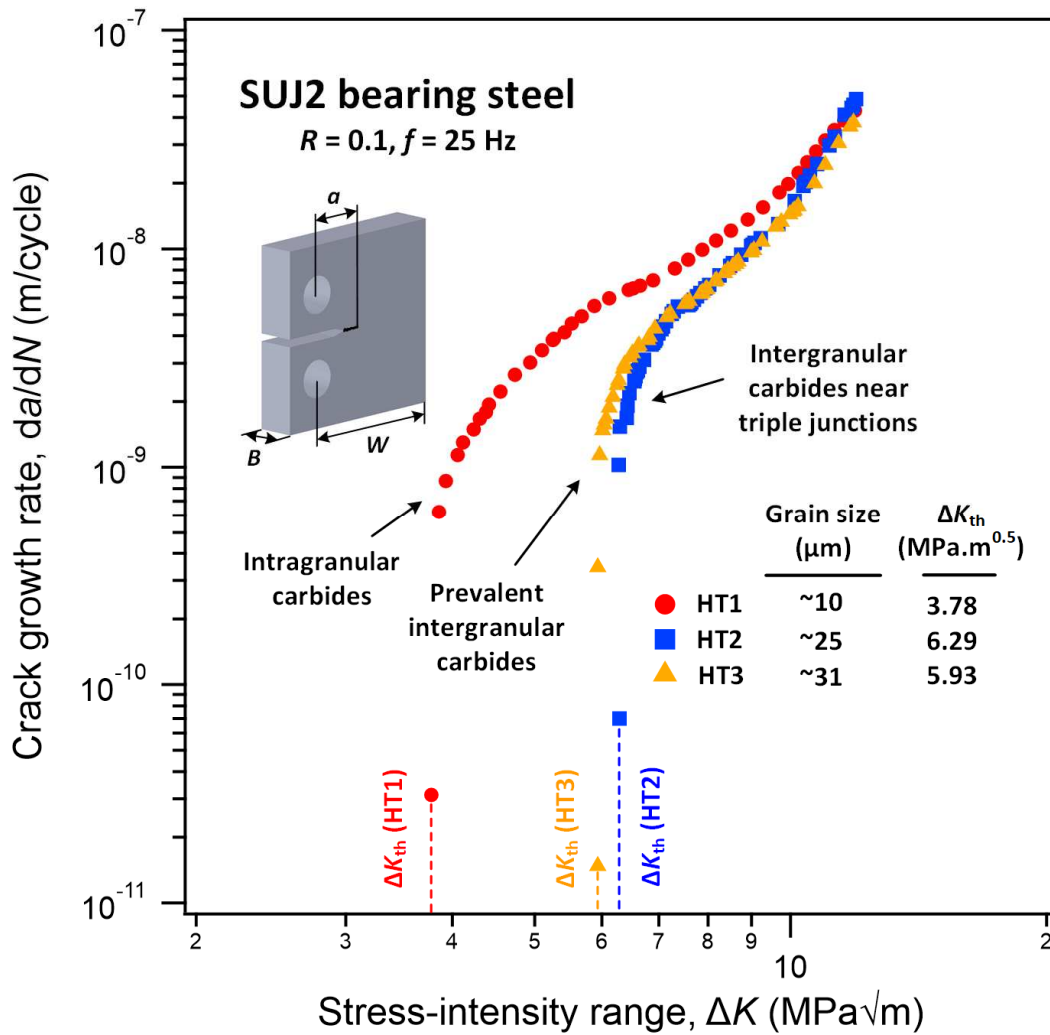


Fig. 5. Variation in fatigue-crack propagation rates, da/dN , as a function of the stress-intensity range ΔK , of the three microstructures in the SUJ2 steel tested at room temperature at an R -ratio of 0.1. The threshold stress-intensity range, ΔK_{th} , can be seen to be improved from $\Delta K_{\text{th}} = 3.78 \text{ MPa}\cdot\text{m}^{1/2}$ in the fine-grained HT1 structure to $\Delta K_{\text{th}} = 6.29 \text{ MPa}\cdot\text{m}^{1/2}$ and $5.93 \text{ MPa}\cdot\text{m}^{1/2}$ in the coarser-grained HT2 and HT3 structures, respectively.

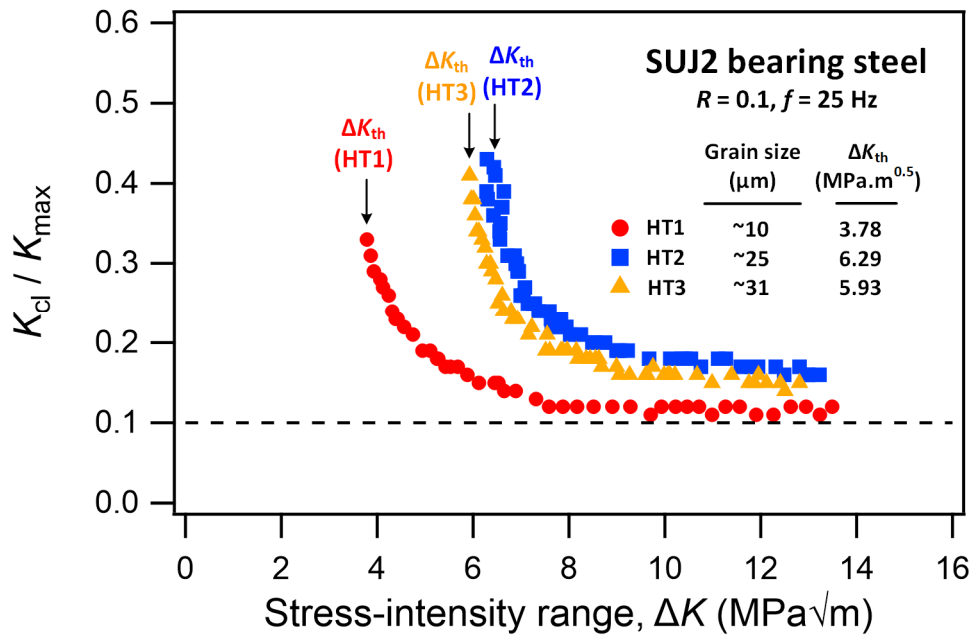


Fig. 6. Variation in the magnitude of crack closure in terms of the ratio of closure stress intensity to the maximum stress intensity (K_{cl}/K_{max}) as a function of the stress-intensity range (ΔK) for the three heat-treated SUJ2 steel microstructures. The effect of crack closure becomes more pronounced as ΔK is decreases into the near-threshold region, which is primarily associated with the smaller crack-opening displacements at low stress-intensity levels. The coarser-grained HT2 and HT3 structures can be seen to display higher levels of crack closure than the fine-grained HT1 structure.

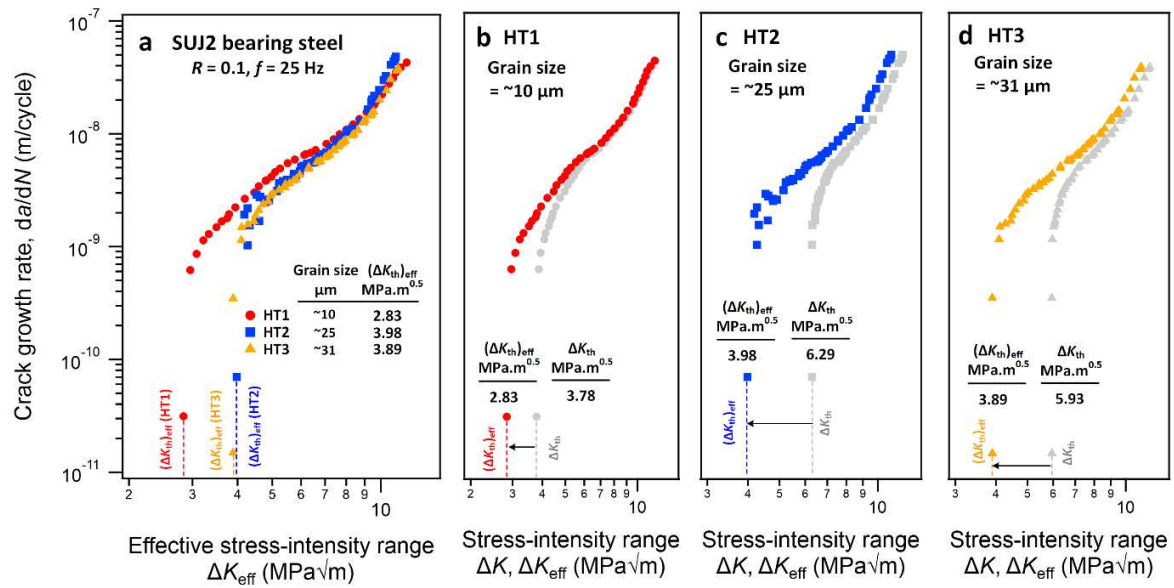


Fig. 7. Fatigue-crack propagation behavior of the three heat-treated SUJ2 steels plotted with da/dN vs. ΔK and ΔK_{eff} . (a) da/dN vs. ΔK_{eff} curves, where $\Delta K_{eff} = K_{max} - K_{cl}$ (when $K_{cl} > K_{min}$). Comparison of the da/dN vs. ΔK_{eff} and da/dN vs. ΔK curves for the (b) HT1, (c) HT2, and (d) HT3 structures. The role of crack closure significantly diminishes the differences in the crack-growth behavior between the three microstructures. Such an effect is particularly pronounced for the HT2 and HT3 structures having coarse grains with similar sizes, leading to a virtual overlap of the da/dN vs. ΔK_{eff} curves.

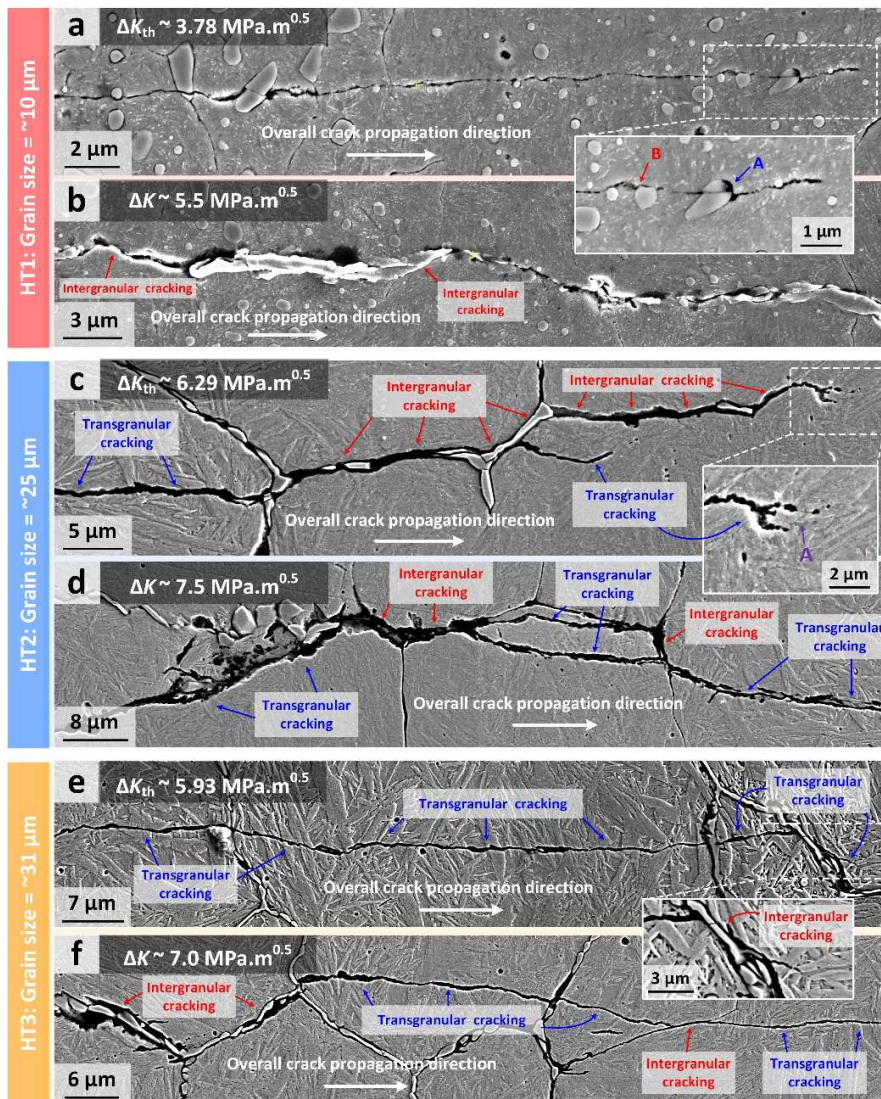


Fig. 8. Secondary electron imaging of the crack-path profiles for the three heat-treated SUJ2 steels. (a) A relatively straight mode-I crack-path profile is displayed for fine-grained HT1 structure near the threshold region, where the crack propagation is driven predominantly by transgranular cracking. (b) Crack propagation in a mixture of transgranular cracking with minor intergranular cracking at the mid-range of growth rates in the HT1 structure. (c) Mixed transgranular and intergranular cracking is observed in the HT2 structure in the near-threshold region. Crack deflection and branching occurs as the crack proceeds through the intersected martensitic lamellae. (d) Mixture of transgranular and intergranular cracking is present in the HT2 structure at the mid-range growth rates. (e) Crack propagation near the threshold regime in the HT3 structure is predominantly transgranular with minor evidence of intergranular cracking. (f) Mixed intergranular and transgranular cracking is observed for the crack-path profile at the mid-range growth rates in the HT3 structure.

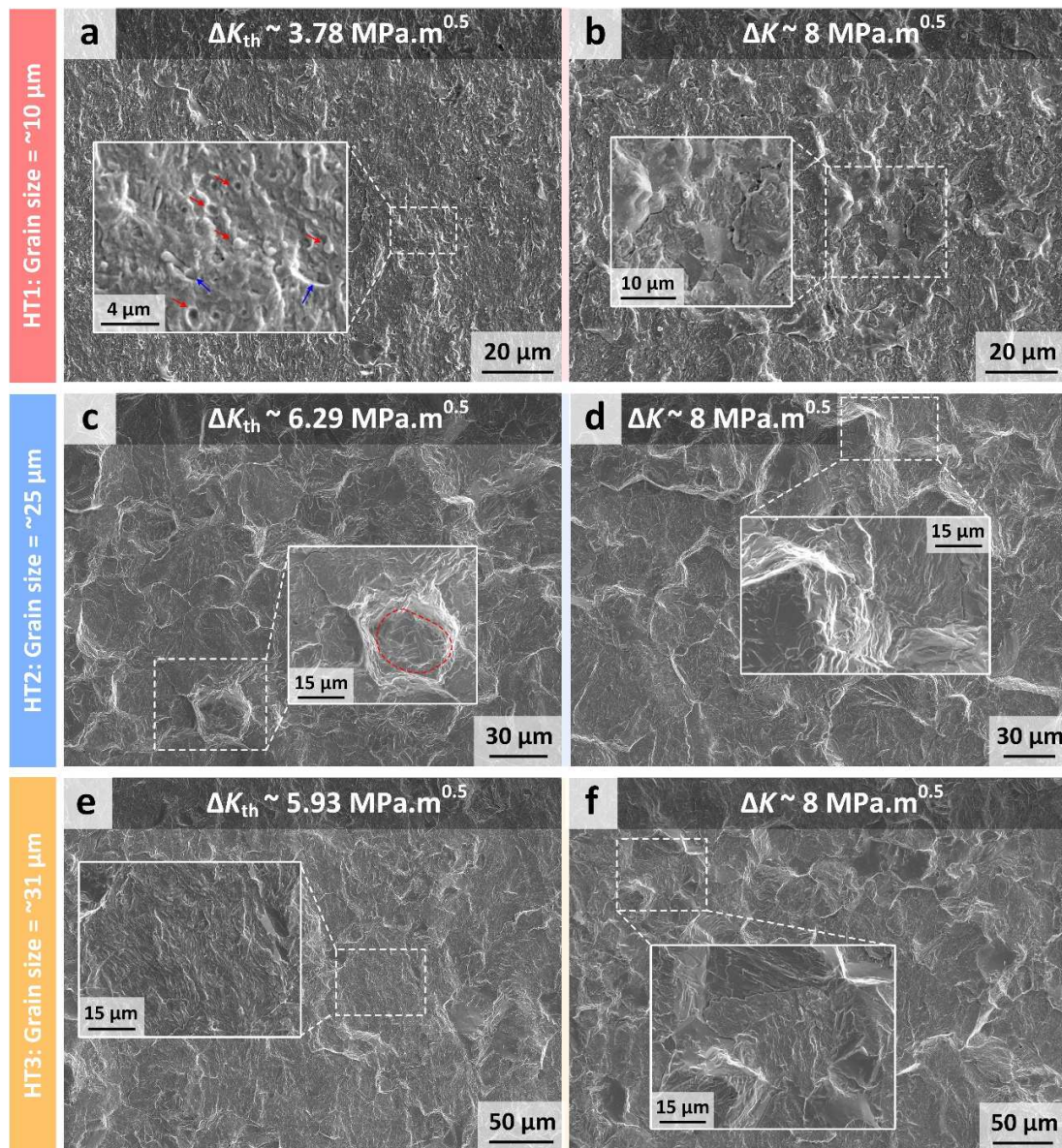


Fig. 9. Fatigue fractography of the three heat-treated SUJ2 steels. (a) Relatively flat surface is resulted from the predominant transgranular cracking near the fatigue threshold region in the HT1 structure. (b) A mixed fracture morphology of transgranular features with minor intergranular features is shown at mid-range growth rates for the HT1 structure. For the coarse-grained HT2 structure, a rough fracture surface showing a mixture of a comparable amount of transgranular features and intergranular features is present (c) near the threshold region as well as (d) at the mid-range of growth rates. (e) The HT3 structure exhibits a relatively flat fracture surface showing mixture of transgranular features with minor intergranular features near the threshold region. (f) At intermediate growth rates for the HT3 structure, a rough surface containing both transgranular features and intergranular features is shown.

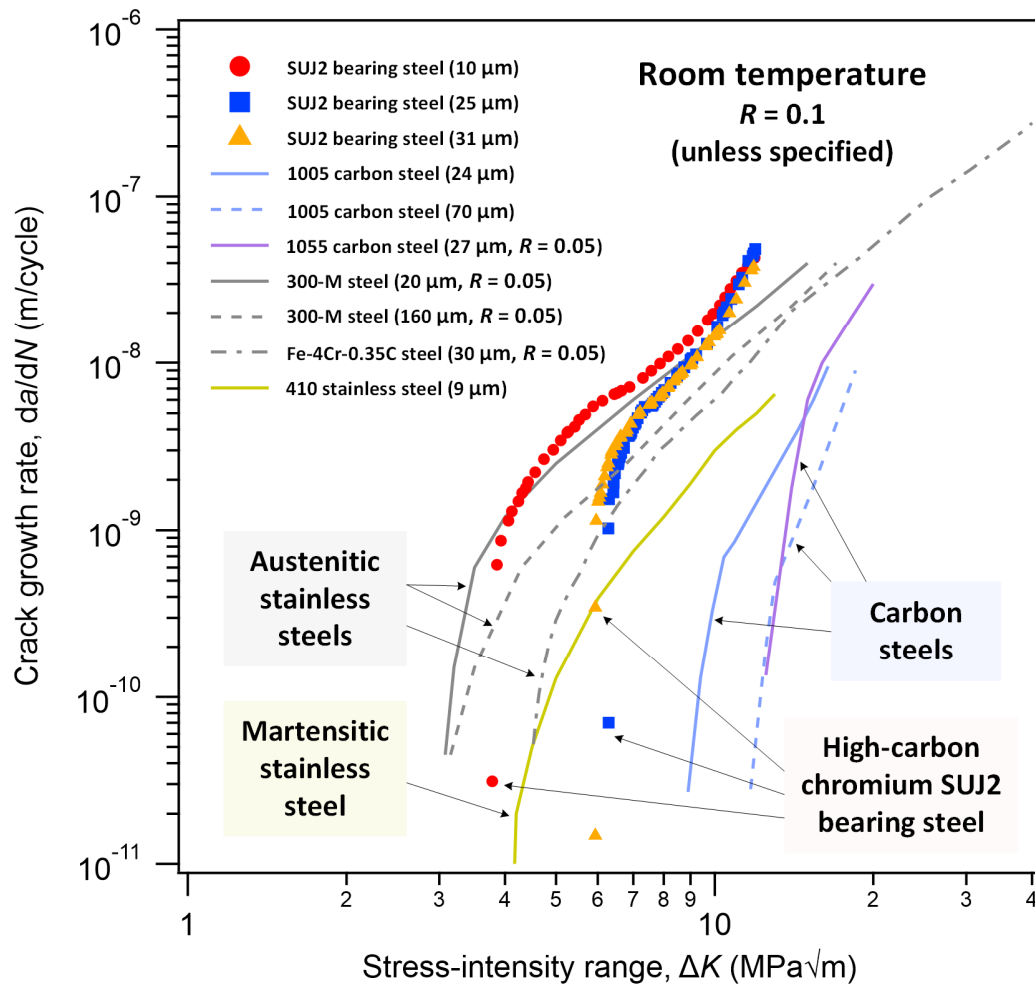


Fig. 10. Comparison of the fatigue-crack growth behavior of the three heat-treated SUJ2 steels with high-strength austenitic and martensitic stainless steels and low-strength carbon steels. The high-carbon chromium SUJ2 bearing steel outperforms the high-strength stainless steels [29-30] and the low-strength carbon steels [27-28] in terms of its combination of strength and fatigue-crack growth performance; despite its lower ductility and toughness, it clearly represents a superior structural alloy for bearing applications.